Simulation Modelling Practice and Theory 124 (2023) 102726

Contents lists available at ScienceDirect

Simulation Modelling Practice and Theory

journal homepage: www.elsevier.com/locate/simpat

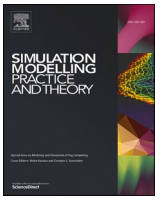

Energy management and control strategy of DC microgrid based hybrid storage system

Hassan Abouobaida [a,*], Lais de Oliveira-Assis [b], Emanuel P.P. Soares-Ramos [c], Hassane Mahmoudi [d], Josep M. Guerrero [e], Mohsin Jamil [f]

[a] Laboratory of Engineering Sciences for Energy (LABSIPE), National School of Applied Sciences (ENSA) El Jadida, Chouaib-Doukkali University. Morocco
[b] National Council for Scientific and Technological Development (CNPq) scholarship hoder, University of Cádiz, Spain
[c] Federal Center for Technological Education of Minas Gerais (CEFET-MG), Department of Electro-electronics, Curvelo, MG, Brazil
[d] Power Electronics, Intelligent Control Techniques and Robotics (EPTICR), Mohammadia School of Engineering, Mohamed V University, Rabat, Morocco
[e] Department of Energy Technology, Aalborg University, DK-9220 Aalborg, Denmark
[f] Department of Electrical and Computer Engineering, Memorial University of Newfoundland, Canada

ARTICLE INFO

Keywords:
Energy management
Sliding control
Photovoltaic
Wind

ABSTRACT

In this paper, a method of energy management shared with storage devices in a standalone DC microgrid is presented. The objective of management is to satisfy the energy demand in addition to guaranteeing a production/consumption balance with good regulation and stability of DC bus voltage. Another advantage of the energy management method lies in the consideration of losses in the static converters by calculating the effective power available on the common DC bus. The proposed control strategy takes advantage of non-linear control by combining fuzzy logic control for the extraction of the maximum power from the photovoltaic and wind sources, while sliding mode control is used for the control of the storage power converters. The control of the power flow of the common DC bus allowed good stability of the bus voltage with small deviations around the desired value, limiting the battery stress since the low-frequency current component is sent to the battery while the higher-frequency power component is directed to the supercapacitor. The simulation results show the validity of the proposed energy management and control strategy.

1. Introduction

Renewable energy systems are continuously gaining more prominence and, as a consequence, contributing to diversify the energy mix. This fact, enhances energy security and it is environmentally friendly [1]. The abundance of the primary sources of energy, especially wind and sun, and the advances in the research / application mainly to produce electricity, constitute advantages of these systems. Photovoltaic (PV) and wind systems have been widely applied in recent years, being the focus of many research papers [2,3]. For instance, the integration of hybrid energy systems for off-grid electrification in developing countries has been analyzed in [4], where a microgrid composed of renewable sources plus a storage system is studied. The feasibility of a microgrid hybrid renewable

* Corresponding author.
E-mail address: hassanabouobaida@gmail.com (H. Abouobaida).

https://doi.org/10.1016/j.simpat.2023.102726
Received 20 August 2022; Received in revised form 5 November 2022; Accepted 14 January 2023
Available online 20 January 2023
1569-190X/

energy system, including the energy generated through solar power, wind power, and a diesel generator connected to a synchronous machine, was studied in [5].

A microgrid can be connected to the utility grid or can work independently in a stand-alone system. The main advantage of a grid-connected system is that it can avoid the need for a storage system, since the grid is able to, compensate the intermittent nature of renewable generation. The authors [6] chose the grid-connected configuration, in which a stability analysis is performed and a renewable PV generation is connected to the grid. With respect to the stand-alone system, the main advantage of this arrangement is the capability to be employed for remote areas with no grid availability, although it is usually more expensive, being the strategy adopted for [7] and [8].

In order to avail most of the PV modules and wind turbines potential, the maximum power point tracking (MPPT) is an important parameter. With the MPPT is possible to achieve higher performance with an appropriate duty cycle of the power converter. The MPPT control can be obtained through different techniques [9,10], being the techniques widely employed for PV systems the perturb and observe (P&O) [11], incremental conductance (INC-COND) [12] and fuzzy logic control (FLC) [13]. When these three methods are compared, the P&O and INC-COND techniques are simpler to implement, however presents some issues under varying solar irradiation. The FLC has a higher precision, whereas a higher computational effort is necessary, due to its greater complexity [14]. These references present each of the mentioned control methods independently, and does not performs a comparison among them, and in this paper, this study is performed. For the wind systems the most popular techniques for the MPPT control are the tip speed ratio, the optimal torque, the power signal feedback and the P&O, in which the P&O highlights due to its simplicity, and the optimal torque due to its accuracy [15].

The fluctuating nature of renewable sources is a challenge which needs to be overcome in order to turn these systems more suitable to integrate in the grid [16]. In this sense, energy storage systems are important elements to deal with the intermittence of renewable generation, acting to sustain the energy demand unpredictability, and thus, allowing to control the power flow according to the necessity of the load / grid. Many storage technologies are found in the literature, among them can be mentioned the batteries, supercapacitors (SC), pumped hydro, flywheel and hydrogen, and each one is preferable depending on the time that is intended to store the energy and the response time [17]. In general, it is interesting to combine a short-term with a long-term storage system in order to obtain the benefits of both systems, which was the strategy presented by the authors in [18]. The authors, combined the use of SC for short-term operation and the hydrogen system for long-term operation, combined with a wind turbine as the main manner of generation. Furthermore, the combination of two storage systems allows a faster contribution to the development of enhanced technologies, in terms of efficiency, durability, response time and a cost reduction [19]. For this reason, in this paper the junction of two storage systems (battery and supercapacitor) is studied, creating a robust system while dealing with intermittence, and supplying uninterrupted power to the loads.

When a hybrid system is being investigated, an important parameter that needs to be considered is a control method, which will guarantee a proper power flow between sources and load. In this regard, a number of literature has been devoted to the study of the control method, and what is possible to infer is that it can be performed using linear [20], nonlinear programming and / or intelligent techniques [21–23].

The most common and well established control method is based on proportional, integral and derivative (PID) method that is based on linear programming and widely applied. For instance, the PID for supervisory control was used by the authors in [18], in which the technique was explained previously, and in [20] the control algorithms are proposed for smooth power transfer between ac and dc links and for stable system operation under various generation and load conditions. In [24], for example, the PI implemented, was studied using simulations as well as HIL verification and compared with other existing power management results, admitting faster DC bus voltage regulation. Another method to improve the system monitoring and performance is the nonlinear sliding mode control (SMC), which demonstrate to be robust to deal with disturbances and parameter variation while presenting a simple structure [25].

Regarding the power management strategies, various methods are possible to be employed in order to control the energy flux. In [26] a system composed of a wind turbine / doubly fed induction generator (DFIG), a PV generator, a fuel cell, an electrolyzer, and a battery bank is studied. In this case, a power management strategy is proposed, consisting of using the surplus energy from the PV and wind systems to perform the water electrolysis in an effort to produce hydrogen and also to store energy in the batteries. The battery and the energy generated by the fuel cell will later be used as a backup generator to provide the required power. Another example, is the use of a new control framework for the optimal energy management of the PV plus battery system under varying operating conditions [27], in which a novel adaptive robust control framework for the optimal energy management of the PV-battery system, subject to unmodeled dynamics, is improved through an exponential-like adaptive integral sliding mode control coupled to a neural network approximator. An energy management system has been developed to govern the power supply to the grid, considering two possible scenarios: 1) system operator command following; or 2) economic dispatch of the stored energy [28]. In [29], real time embedded system energy management is developed and examined for an autonomous hybrid system.

Hybrid renewable energy systems (HRES) with storage systems are interconnected through power converters. The converters are responsible for adjusting the voltage levels and controlling the power flow between sources, storage systems, and loads. To connect loads to direct current (DC), DC / DC converters are generally used, working as boost or buck converters, increasing or reducing the voltage level, respectively. Different topologies of DC / DC converters are proposed in [30]. Alternating current (AC) loads are usually connected using a voltage source inverter (VSI) [31]. The average version of the converters is characterized by the simplification of the simulation process and also by controller analysis [32], which is an interesting model to be considered. Regarding the control, pulse width modulation (PWM) is a technique widely applied in power electronics [33] in which, by varying the pulse width, it is possible to vary the amount of power delivered to the load / grid.

In this paper, an energy management system for a DC microgrid composed of wind turbines, PV generation, batteries, SC, and AC / DC loads is proposed. The objective is to reach a power balance between the sources, the storage system, and the loads, satisfying the

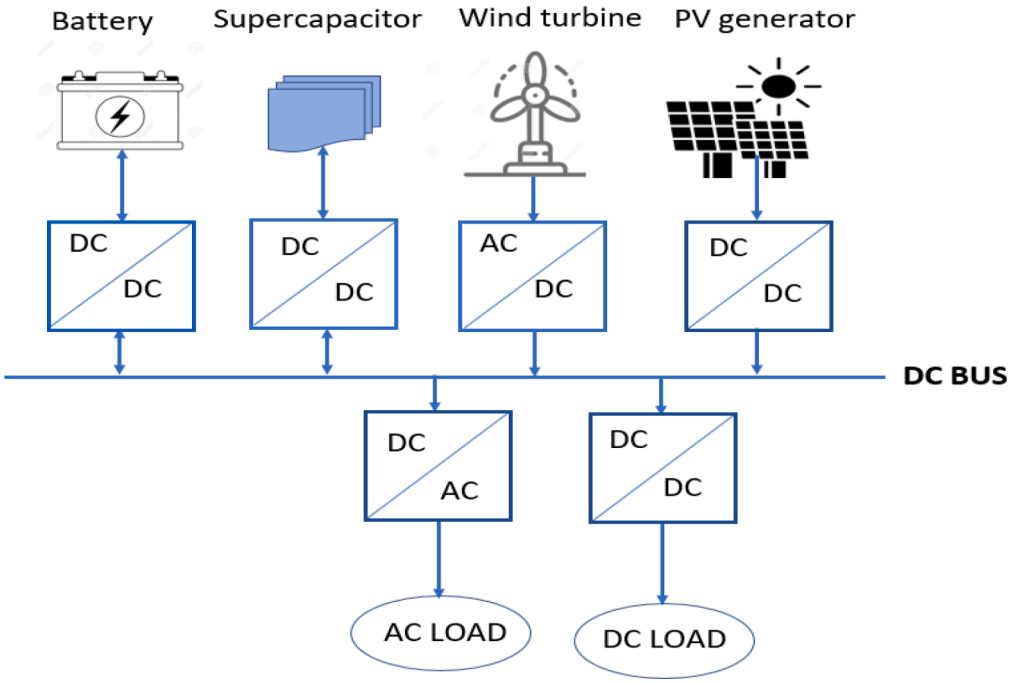

Fig. 1. Configuration of the DC microgrid.

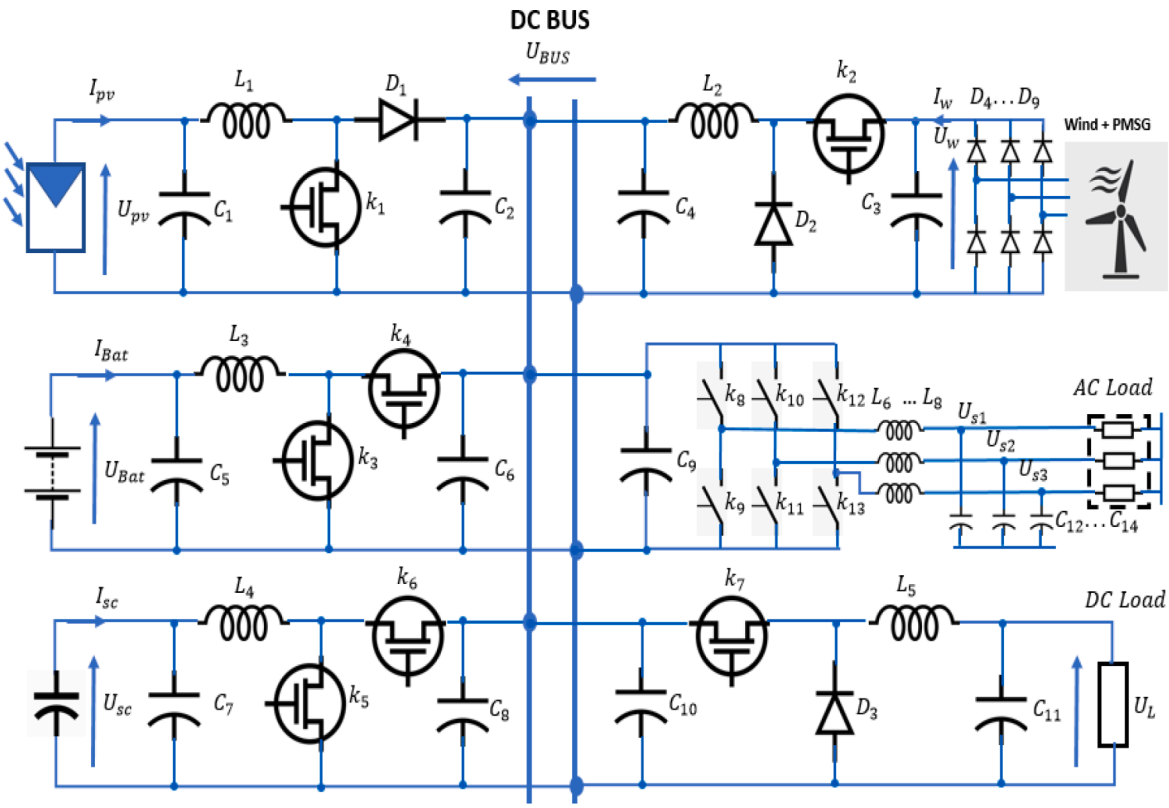

Fig. 2. Configuration of the microgrid.

energy demand while regulating the DC bus voltage with an improved deviation and low battery stress. A comparison between the control methods for the MEM using PID, PID - SMC combined with SMC is simulated and presented. Three methods (P&O, INC-COND, and FLC) were used and compared to detect the optimal power point. Boost, buck, and bidirectional converters were considered in this study, and the losses in this equipment were also presented. A low voltage distortion was obtained on the AC side.

This paper is organized as follows: In section II, the system configuration and modelling are described. Section III describes the power management and control. In Section IV the results and discussion are presented, followed by the conclusions in section V.

2. System configuration and modeling

Fig. 1 shows the topology of the standalone DC microgrid system implemented in this paper. The described system has two renewable energy sources, a PV panel and a wind turbine. Furthermore, an energy storage system (battery and SC) has been inserted to solve the problem of intermittence and improve the controllability of these renewable sources. In addition, the topology enables AC and DC loads connection. The AC load is connected through a VSI with a LC filter, while the DC load is connected through a buck converter. Fig. 2 shows in detail the electrical diagram of the DC microgrid. In the following sections, the study focuses on the autonomous microgrid .

2.1. Photovoltaic and wind turbine models

The PV array has an output voltage of 203 V, with a rated power of 1.48 kW, and thus the PV plant is connected to the DC bus through a boost converter. The model applied to the PV system is shown in [34]. The model consists of a diode, a controlled current source, a series and a shunt resistor. In addition, irradiance and temperature are the input parameters, whereas the output parameters are the voltage and current. According to [35], this model is accurate and simple to implement. The equations to find the output current are available in Eqs. (1) - (3).

$$I_{pv} = I_L - I_{sat}\left(e^{q\frac{(V_{pv}+I_{pv}R_s)}{NkT_{pv}}} - 1\right) - \frac{\left(V_{pv} + I_{pv}R_s\right)}{R_{sh}} \tag{1}$$

$$I_L = (I_{L0} + K_0(T - T_n)) \cdot \frac{G}{G_n} \tag{2}$$

$$I_{sat} = I_{sat,n}\left(\frac{T_n}{T}\right)^3 e\left[\frac{qE_g}{ak}\left(\frac{1}{T_n} - \frac{1}{T}\right)\right] \tag{3}$$

where I_{L0} is solar-induced current at STC condition, I_L is solar-induced current (A), respectively; $I_{sat,n}$, I_{sat} is the nominal saturation current of the diode at STC condition and the saturation diode current (A); Boltzmann constant ($J{\cdot}K^{-1}$) is represented by k; the elementary charge of an electron (C) is represented by q; K_O is a constant thermal coefficient depending on the PV characteristic; T and T_n is the operating and the nominal temperature (25°C) of the PV; Eg is the bandgap energy of the semiconductor (eV); a is the diode ideal constant; R_{sh} and R_s are the shunt resistance and series resistance (Ω), respectively; and G and G_n are the irradiation and the nominal irradiation (1000 W/m^2) on the device surface, respectively.

Usually fundamental frequency simulations studies, the wind turbine can be represented by three subsystems: rotor, drivetrain and generator system. The wind turbine rotor is modelled by the quasi-static model defined through the actuator disk theory, and the drive train is represented by the two-mass model, as usual in fundamental frequency simulations [36]. The wind turbine generator based on a permanent magnet synchronous generator (PMSG) has a rated power of 1.5 kW and it is connected to the DC bus through an AC / DC converter. Typically, a full-scale power converter which is composed of the three-phase uncontrolled bridge rectifier is applied in the first stage of conversion, while witch in the second stage a DC / DC buck converter is used to connect the PMSG to DC bus.

The equations Eqs. (4) - (10) refers the wind turbine and PMSG model. The rotor model define the mechanical power (P_m) Eq. (4)) extracted from the wind is modelled by the quasi static approach of the actuator disk theory [36]. The tip speed ratio (λ) is the ratio between blade tip linear speed and the wind speed is defined in Eq. (5). The power coefficient (C_p) is given in Eq. (6), λ_i is given by Eq. (7). The PMSG generator was modelled using the equations Eqs. (8) - ((10) of the synchronous dq reference [37], assuming that the flux distribution in the stator is sinusoidal through a three-phase model.

$$Pm = c_p(\lambda, \beta)\frac{\rho\pi r^2}{2}v_{wind}^3 \tag{4}$$

$$\lambda = \frac{\omega_t \cdot r}{v_{wind}} \tag{5}$$

$$C_p(\lambda, \beta) = 0.5176 \cdot \left(\frac{116}{\lambda_i} - 0.4 \cdot \beta - 5\right) \cdot e^{-\frac{21}{\lambda_i}} + 0.0068 \cdot \lambda \tag{6}$$

$$\frac{1}{\lambda_i} = \frac{1}{\lambda + 0.08 \cdot \beta} - \frac{0.035}{\beta^3 - 1} \tag{7}$$

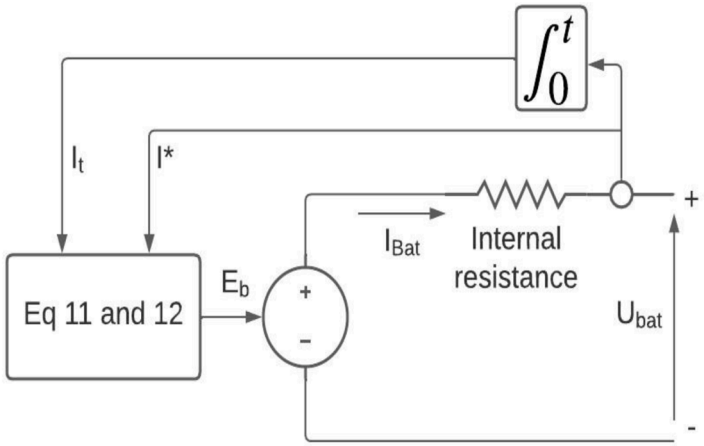

a)

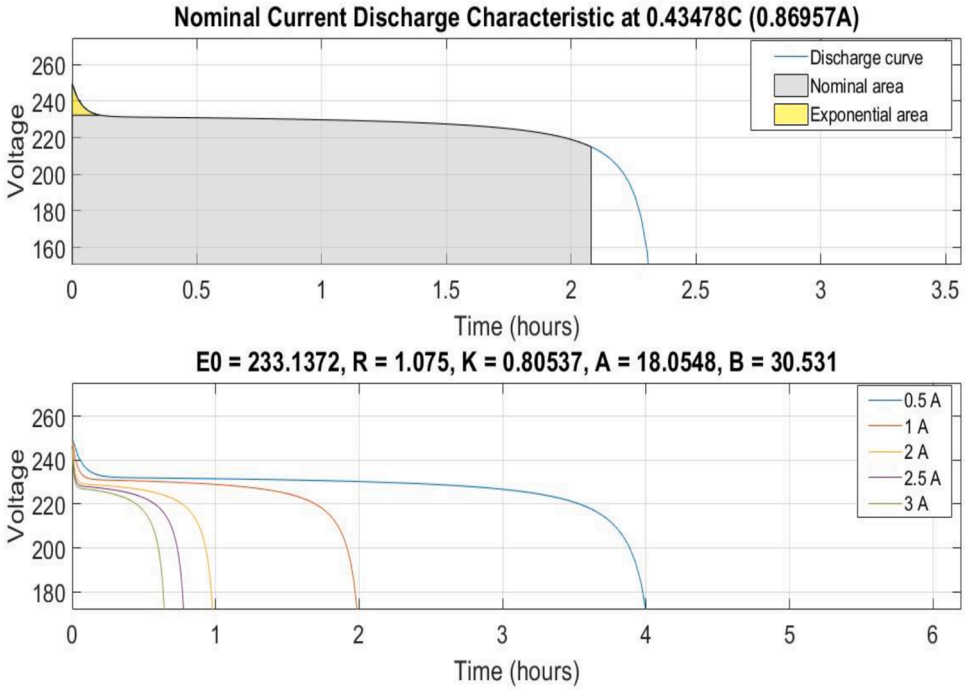

b)

Fig. 3. a) Equivalent circuit of the battery; b) The discharge curves characteristics.

$$U_{ds} = R_s i_{sd} + L_d \frac{di_{ds}}{d_t} - \omega_e L_q i_{qs} \tag{8}$$

$$U_{qs} = R_s i_{sq} + L_q \frac{di_{qs}}{d_t} + \omega_e \left(L_d i_{ds} + \phi_{pm}\right) \tag{9}$$

$$T_e = \frac{3}{2} P_p \left(\phi_{pm} i_{qs} + \left(L_d - L_q\right) i_{ds} i_{qs}\right) \tag{10}$$

where ρ is the air density; $A(\pi r^2)$ is the area swept by the rotor; v_{wind} is the wind speed; ω_t is the rotation speed (rad/s); r is the rotor radius of the wind turbine; β is the pitch angle; d and q are the direct and quadrature components, respectively; index s refers to stator; L_s and R_s are the stator inductance (H) and stator resistance (Ω), respectively; u and i denote voltage (V) and current (A), respectively; ω_e is the electrical speed (rad/s); ϕ_{pm} is permanent magnetic flux (Wb); T_e is the electromagnetic torque; and P_p is the number of pole pairs.

2.2. Battery and supercapacitor

The application of energy storage on systems that have intermittent sources is an interesting way in order to attenuate this characteristic. Several storage systems are discussed in [38], and a widely accepted alternative is the battery. The Lithium-ion batteries, has good life-cycle, high efficiency, deep discharge depth and fast charging [39] and due to these advantages, was applied in this paper. The model available in Simulink SimPowerSystems toolbox composed by a variable voltage source and a resistance connected in series is accurate, and thus, was the model used in this paper. An equivalent circuit simplified is shows in Fig. 3a. For the battery of the lithium-ion battery type, the charge equation (i* < 0) is given as Eq. (11) and discharge equation (i* > 0) is given as Eq. (12). The discharge curves characteristics of the BES can be seen in Fig. 3b.

$$f_2(it, i*, i) = E_0 - K \cdot \frac{Q}{it + 0.1 \cdot Q} \cdot i* - K \cdot \frac{Q}{Q - it} \cdot it + A \cdot \exp(-B \cdot it) \tag{11}$$

$$f_1(it, i*, i) = E_0 - K \cdot \frac{Q}{Q - it} \cdot i* - K \cdot \frac{Q}{Q - it} \cdot it + A \cdot \exp(-B \cdot it) \tag{12}$$

Where E_0 is the constant voltage (V), K is the polarization constant (V/Ah) or polarization resistance (Ω), i* is the low-frequency current dynamics (A), i is the battery current (A), it is the extracted capacity (Ah), Q is the maximum battery capacity (Ah), A is the exponential voltage (V), B is the exponential capacity (Ah^{-1}).

The battery output voltage (U_{bat}) can be obtained through Eq. (13).

$$U_{Bat} = E_b - I_{Bat} \cdot R_{\text{int}} \tag{13}$$

where E_b is the open circuit voltage of the battery (V), which depends on if the battery is charging or discharging, R_{int} is the internal resistance (Ω) and I_{Bat} is the battery current (A). State of charge (SOC) is an important parameter of the battery, that is necessary to be controlled to avoid a great discharge and an over charge. The SOC is represented in Eq. (14).

$$SOC(t) = SOC_0 + \frac{1}{C_{nom}} \int I_{Bat}.dt \tag{14}$$

where SOC_o is the initial state of charge, C_{nom} is the battery nominal capacity (Ah) given by manufactures and I_{Bat} is the battery current (A). The parameter specifications of the renewable sources, filters and storage systems are given in Table 3.

The SC was modelled according [40], this model is an adequate representation for describing the SC performance in several applications. Like a conventional capacitor, the SC is an electrostatic device with a high capacitance, being able to reach 100 to 1000 times the capacitance per unit volume compared to a conventional electrolytic capacitor.

2.3. DC/DC converters

For a hybrid system operates in an appropriate manner, power converters are required. The converters are necessary for adjusting the voltage levels and controlling the power flow between the elements involved in the HRES. Several ways such as, average steady-state model and dynamic small-signals representation, can be applied for the study of the converters. In this section, the buck, boost and buck-boost model converter are discussed. Fig. 2 shows the converters applied in this paper, with its respective variables.

2.3.1. Buck converter

The DC/DC buck converter control associated with the wind turbine source, uses FLC and ensures maximum power operation of the wind turbine. The wind DC/DC buck converter control allows to regulate the output voltage of the rectifier bridge at a voltage of 620 V for a wind speed of 12 m/s. The peak wind power delivered to the DC bus is 1.5 kW. Similarly, another DC/DC buck converter is connected between the DC bus and the DC load with an resistance equals to 30 Ω. This converter ensures the regulation of the voltage at

the terminals of the DC load at 200 V, which allows to deliver an average power of 1.33 kW.

The buck converter operates in closed loop to adjust the source voltage level to connect to the DC bus. This converter is used for reducing the voltage. The operation principle is based on the switching of the switch number 2 (k_2), within a time period T_s. Note that the switches are named from 1 to 13 ($k_{1\text{-}13}$), as presented in Fig. 2. For the buck converter connected to the wind source, when the k_2 is turned-on, the bus receives energy from the wind source (U_w), through the inductor (L_2) and capacitor (C_4), in other hand, when k_2 is turned-off, the bus is supplied through the freewheeling diode (D_2), with the remaining energy of the L_2 and C_4. Note that k_2 is equal to k_7, being k_2 the buck converter switch in which the wind source is connected, and k_7 refers to the switch in which the DC load is connected. For the buck converter connected to the DC load, the working principle is the same that for the wind source converter, however it operates in reverse mode, with the energy flowing from the DC bus to the load through of the inductor (L_5) and capacitor (C_{11}). The equations that refers to this model and the operation mode is given in [41]. The average buck converter models associated with the wind source and the DC load are given by Eqs. (15) - (16).

$$\begin{cases} L_2 \dfrac{dI_{L_2}}{dt} = \alpha_2 U_w - U_{Bus} \\ C_4 \dfrac{dU_{Bus}}{dt} = I_{L_2} - I_{o2} \end{cases} \tag{15}$$

$$\begin{cases} L_5 \dfrac{dI_{L_2}}{dt} = \alpha_7 U_{Bus} - U_L \\ C_{11} \dfrac{dU_{Bus}}{dt} = I_{L_5} - \dfrac{U_L}{R_L} \end{cases} \tag{16}$$

where U_{bus}, U_w and U_L are low - frequency averaged values of DC bus voltage, voltage at the output of the uncontrolled rectifier applied to the wind turbine and load voltage DC, respectively. Where α_2 and α_7 are the duty cycles of the switches (k_2, k_7). I_{L2}, I_{L5} and I_{o2} are inductor currents (L_2, L_5), and output current, respectively. The voltages, currents and modulating signals are time-dependent variables, however, the "t" is hidden in the equations for notation simplicity.

2.3.2. Boost converter

Such as the wind buck converter, the boost converter is designed to maximize the power delivered by the PV source. The maximum power of this converter is 1.48 kW when the temperature is 25°C and the irradiation is 1000 W/m^2. In the closed loop, the photovoltaic MPPT operating is based on a FLC, the generated duty cycle is through the PWM to regulate the voltage at the terminals at 203 V under the above mentioned conditions. The equations of DC/DC boost, it means, the differential equations for inductor voltage and capacitor current are given by Eq. (17):

$$\begin{cases} L_1 \dfrac{dI_{L_1}}{dt} = U_{pv} - (1 - \alpha_1) U_{Bus} \\ C_2 \dfrac{dV_{C_2}}{dt} = (1 - \alpha_1) I_{L_1} - I_{o1} \end{cases} \tag{17}$$

where U_{pv} is average values of the PV voltage, α_1 are the duty cycle of the switch (k_1). I_{L1} and I_{o1} are inductor current (L_1) and output current respectively.

2.3.3. Bidirectional converter

Bidirectional buck-boost DC/DC converters (Fig. 2) are commonly applied to adjust voltage levels in applications requiring bidirectional power flow, such as electric vehicle and storage systems (SC and batteries). This converter has low cost, few components and high efficiency [42]. Differently of the buck and boost converter, bidirectional DC/DC converters have two controlled switches (k_3 and k_4). Note that k_3 is equal to k_5 and k_4 is equal to k_6, being k_3 and k_4 the bidirectional DC/DC converter switches in which the battery is connected, and k_5 and k_6 refers to the switches in which the SC is connected. The operating principle is the same as in the previous boost and buck converters, however it is necessary to operate two switches (k_3 and k_4) instead of one, to obtain an adequate energy flow between the components and DC bus.

Bidirectional DC/DC converters can operate in two modes. When the switch k_3 is being controlled and k_4 remains turned-off, it is working as a boost, and when the opposite occurs, it is working as a buck converter. In boost mode operation, k_3 is conducting and in this case the converter is injecting energy into the bus, thus, the energy flows from the battery (SC, in the case of the k_5 and k_6) to the DC bus. When k_4 is conducting, the converter is operating as a buck converter and absorbs energy from the DC bus, thus, the energy flows from the DC bus to the battery. The equations for this converter are the same as those previously expressed, changing according to the mode of operation.

The control of the converters associated with the battery/SC consists of two loops, an external loop for the voltage regulation and an internal loop for the current regulation. The control of the bidirectional converters ensures the regulation of the DC bus voltage at 400 V, a control of the power flow delivered or absorbed from the DC bus by ensuring the battery current regulation, and also a control the power flow delivered or absorbed from the DC bus by ensuring the regulation of the SC current.

In this paper, a SMC is used for the bidirectional converters. The SMC control is adopted using the equivalent average model of the bidirectional converters, that presents a nonlinear behavior which justifies the choice of the SMC that is suitable to this kind of

converter.

The average equivalent model of buck-boost converters is given by Eqs. (18) - (19):

$$\frac{dI_{Bat}}{dt} = \frac{U_{Bat}}{L_3} - \alpha_{34}\frac{U_{Bus}}{L_3} \tag{18}$$

$$\frac{dI_{SC}}{dt} = \frac{U_{SC}}{L_4} - \alpha_{56}\frac{U_{Bus}}{L_4} \tag{19}$$

where U_{Bat}, I_{Bat} are the battery voltage and current, U_{sc}, I_{sc} are the SC voltage and current. U_{BUS} is the voltage in the DC bus. α_{34}, α_{56} are the duty cycles of the switches (k_3, k_4) and (k_5, k_6).

2.4. Voltage source inverter

The three-phase VSI is inserted between the DC bus and the three-phase AC load. The equivalent model of the VSI that is widely used in the literature can be found in [31].

3. Method of energy management

Energy management is based on the calculation of the effective power produced and extracted from a common DC bus, as presented in the following system power balance subsection. Another important parameter to be considerate is the determination of the effective powers taking into account the losses of various static converters.

3.1. System power balance

The power produced by the PV source is given in Eq. (20), while that, the power produced by the wind source at the buck converter input can be calculated according to Eq. (21).

$$P_{pv} = U_{pv} \cdot I_{pv} \tag{20}$$

$$P_{w} = U_{w} \cdot I_{w} \tag{21}$$

where P_{pv}, U_{pv} and I_{pv} are respectively the power, voltage and current in the PV panels. P_w, U_w and I_w are respectively the wind power, voltage and current.

The powers injected by the PV and wind source into the DC bus are expressed through Eq. (22) and Eq. (23), respectively.

$$P_{pv_{DC}} = \sigma_{Boost} \cdot P_{pv} \tag{22}$$

$$P_{w_{DC}} = \sigma_{Buck_1} \cdot P_{w} \tag{23}$$

Where P_{PVDC} and P_{wDC} are respectively the effective powers injected by the PV and wind sources into the DC bus. σ_{Boost} and σ_{Buck1} are the boost and buck converter efficiency.

The effective power produced by the sources and available in the DC bus (P_{SDC}) is given by Eq. (24):

$$P_{S_{DC}} = \sigma_{Boost} \cdot P_{pv} + \sigma_{Buck_1} \cdot P_{w} \tag{24}$$

The powers extracted or consumed from the DC bus, can be in DC or AC. The power consumed by the DC load (P_{L1}) is expressed by Eq. (25) and the power consumed by the AC load (P_{L2}) is expressed by Eq. (26):

$$P_{L_1} = U_L \cdot I_L \tag{25}$$

$$P_{L_2} = \sqrt{3} \cdot U_S \cdot I_S \cos\varphi \tag{26}$$

Where U_L, I_L are the voltage across the DC load and the current through it. U_s and I_s are respectively the voltage between phase and neutral at the terminals of the AC load and the current flowing through it, while $cos\varphi$ is the load angle.

Considering the losses in the buck converter and in the VSI for the power consumed by the DC and AC loads, respectively, the power extracted from the DC bus (P_{LDC}) is given by Eq. (27), where σ_{Buck2} and $\sigma_{inverter}$ are the buck converter and the three - phase inverter efficiencies. The effective power available in excess or deficit in the DC bus (P_{DC}) and shared with the storage devices is given by Eq. (28).

$$P_{L_{DC}} = \frac{P_{L_1}}{\sigma_{Buck_2}} + \frac{P_{L_2}}{\sigma_{Inverter}} \tag{27}$$

$$P_{DC} = \sigma_{Boost} \cdot P_{pv} + \sigma_{Buck_1} \cdot P_{w} - \frac{P_{L_1}}{\sigma_{Buck_2}} - \frac{P_{L_2}}{\sigma_{Inverter}} \tag{28}$$

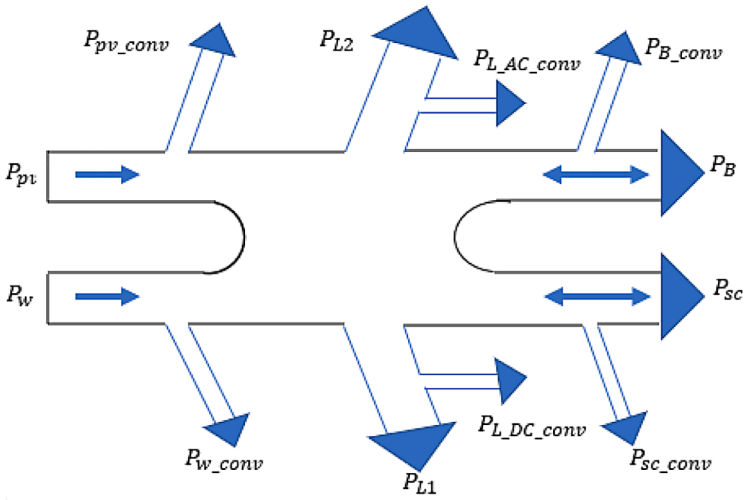

Fig. 4. Power balance of the DC microgrid.

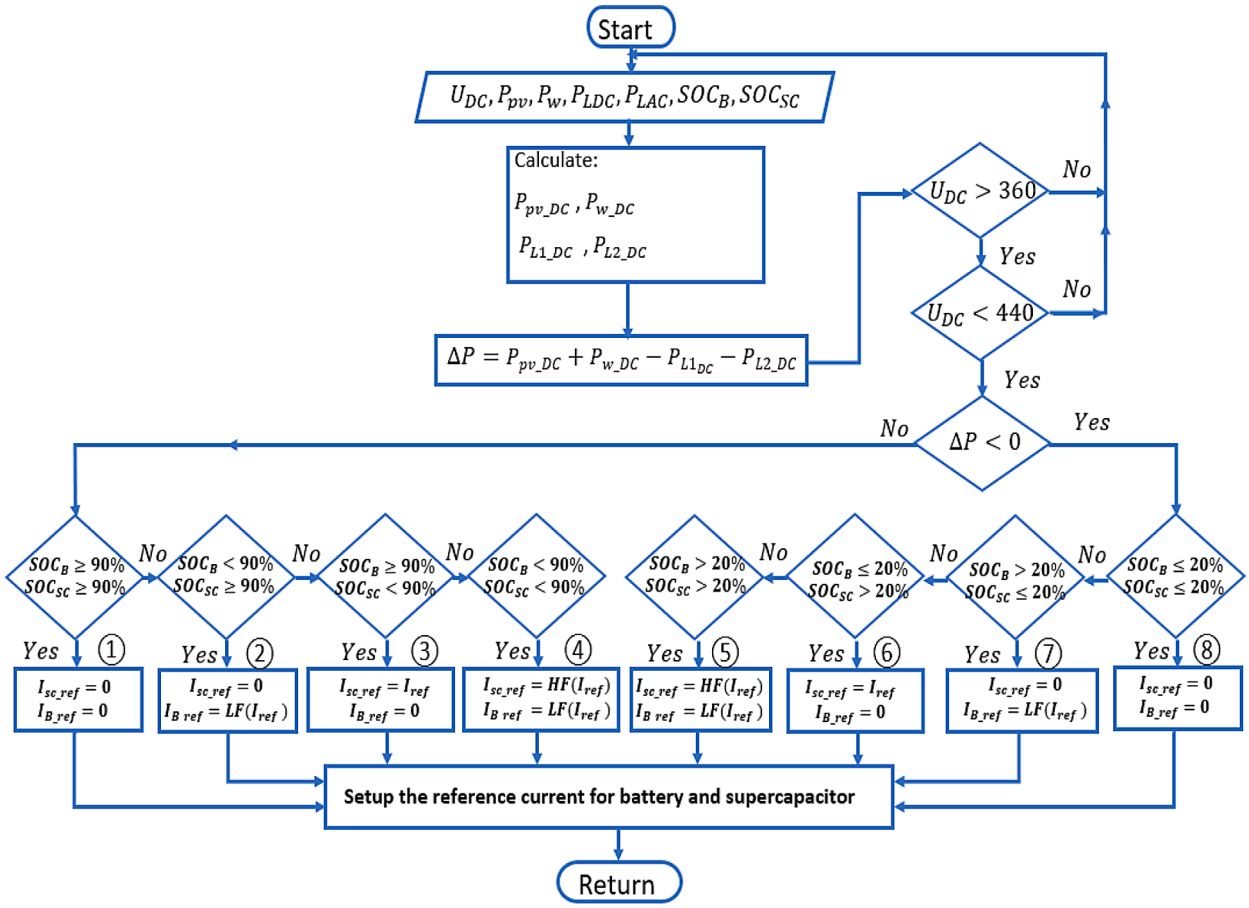

Fig. 5. Energy management algorithm.

Regards to the charging and discharging powers of the storage devices, the power in the batteries (P_B) is expressed by:

$$P_B = U_{Bat} \cdot I_{Bat} \tag{29}$$

where U_{Bat}, I_{Bat} are respectively the voltage and the current of the batteries.

Considering the losses in the bidirectional DC/DC converter, the power extracted or supplied by the batteries from the DC bus is given by Eq. (30).

$$P_{B_{DC}} = \frac{P_B}{\sigma_{rever_1}} \tag{30}$$

where σ_{rever1} is the efficiency of the reversible converter controlling the charge/discharge of the batteries. Likewise, the charge or discharge power of SC is given by Eq. (31).

$$P_{SC} = U_{SC} \cdot I_{SC} \tag{31}$$

where U_{sc}, I_{sc} are respectively the voltage and the current of the SC.

Considering the losses in the bidirectional DC/DC converter, the power extracted or supplied by the SC from the DC bus is given by Eq. (32), where σ_{rever2} is the efficiency of the reversible converter controlling the charge/discharge of the SC.

$$P_{SC_{DC}} = \frac{P_{SC}}{\sigma_{rever_2}} \tag{32}$$

The effective power extracted or injected by the storage devices into the DC bus is obtained through Eq. (33).

$$P_{storage_{DC}} = \frac{P_B}{\sigma_{rever_1}} + \frac{P_{SC}}{\sigma_{rever_2}} \tag{33}$$

Fig. 4 represents the power balance of DC microgrid, being possible to observe the inputs and outputs variables.

3.2. Method of energy management of the DC microgrid system

The MEM is based on measuring the effective power available in the DC bus. The power balance is achieved by calculating the difference between the effective power produced by the PV and wind sources and the power demanded by the loads (Fig. 4), as described in the previous Section 3.1. The energy management is given through Fig. 5, which shows the flowchart of the MEM. When the DC bus voltage is within a margin of 10% around the DC bus voltage of 400 V, it means in the interval of 360 V and 440 V, the energy management starts. The maximum charge and discharge levels of the storage devices are set at 90% and 20%, respectively. For the MEM, two cases are considered, one with extra power and the other with a power deficit, as detailed in the sequence:

Case 1: In the presence of surplus power, four modes are possible depending on the batteries and SC SOCs:

Mode ①

In this mode, the load requirements are met, and the battery and the SC have a high SOC. To reduce the energy production, the MPPT control is stopped for the PV source, and if the same situation (excess power) persists, the MPPT control for the wind source is also stopped.

Mode ②

The energy demands of the loads are satisfied, the SC SOC reaches the high level, so the management system stops charging the SC. The excess power charges the battery as long as the charge level remains below the maximum permitted level.

Mode ③

In mode 3, the batteries are fully charged to their maximum authorized level. The control disconnects the batteries by imposing a zero-reference charge current on them. The SC has a SOC below the maximum value, and the excess power is totally sent to charge the SC.

Mode ④

In the presence of excess power, the charge levels of the batteries and SC are simultaneously lower than the maximum authorized levels. The low-frequency current component charges the batteries, and the high-frequency current component is directed to charge the SC.

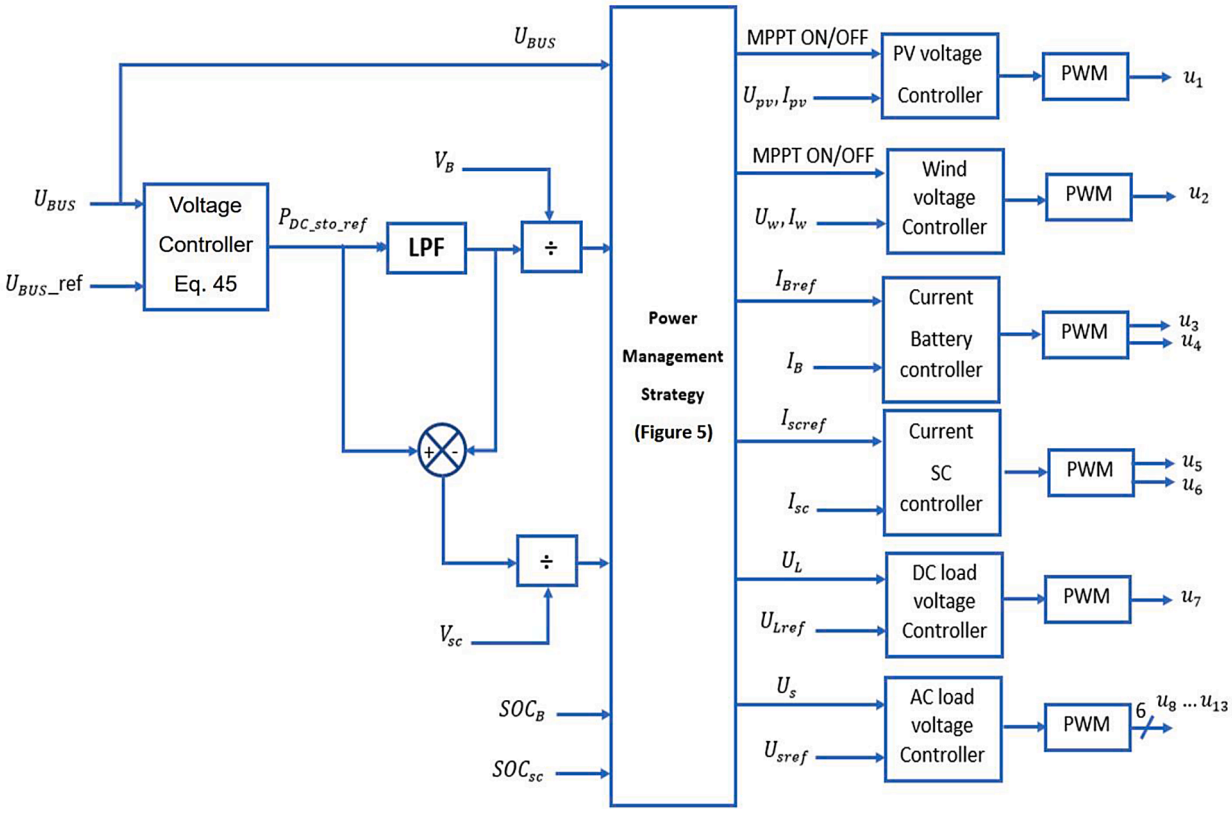

Fig. 6. Control strategy.

Case 2: In the event of a power deficit, four operating modes are distinguished:
Mode ⑤

In this mode, the batteries and SC SOC are above the authorized lower level. To meet the energy needs, the storage devices are discharged.

Mode ⑥

When the battery SOC reaches the lower level, the SC supplies the power requirement.

Mode ⑦

The SC reaches their lowest charge levels and the discharge is stopped. The batteries have a charge level above the lower level and they continue to discharge to satisfy the power demand.

Mode ⑧

The batteries and the SC SOC are simultaneously below the authorized lower level. The discharge of the storage devices are stopped.

4. Microgrid control strategy

The energy management algorithm and microgrid control strategy are illustrated in Fig. 5 and Fig. 6, respectively. In this section, the control strategy of the DC microgrid is presented. The control and energy optimization of the sources (PV, wind) is performed by a FLC (fuzzy logic control). The SMC synthesis is detailed for the control of power flow of the storage devices to the DC bus, in addition to the control of power delivered to the DC load. At the end of this section, the control principle of the three-phase inverter supplying the AC load is presented.

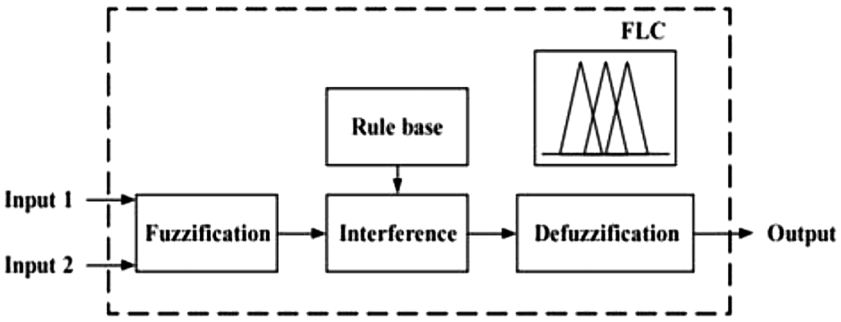

Fig. 7. Components of a fuzzy logic controller.

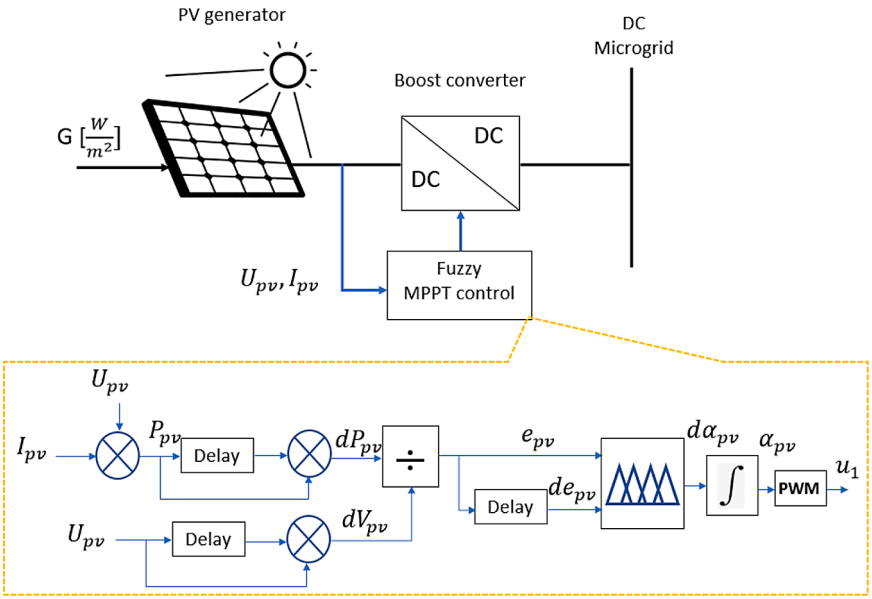

Fig. 8. MPPT control of PV source based FLC.

Table 1
Rules for PV fuzzy logic control.

e_k / de	NB	NS	ZE	PS	PB
NB	NB	NB	NB	NS	ZE
NS	NB	NB	NS	ZE	PS
ZE	NB	NS	ZE	PS	PB
PS	NS	ZE	PS	PB	PB
PB	ZO	PS	PB	PB	PB

4.1. PV and wind source control

The renewable energy sources (PV, wind) are characterized by a rated power of 3 kW and are controlled to operate at their maximum power point (MPP) depending on irradiation levels, temperature, and wind speed. The control of the MPP of the boost and buck converters associated respectively with the PV and wind energy sources, considers the common DC bus voltage, which is fixed at 400 V. The wind and PV source specifications are given in Table 3. Three different MPPT algorithms are tested in Section 5, and these algorithms are: FLC, P&O, and INC-COND MPPT. In the case of the P&O and INC-COND algorithms used to generate the voltage reference signal to be regulated, the synthesis of the PID correctors are necessary for the stability study and the generation of the control law. The FLC principle control is presented in Fig. 7.

The input variables of the FLC are the error (e_k) and the derivative of the error (d_e). The output variable of the FLC is the duty cycle variation. The expressions of these variables are given by the following relations of Eq. (34) and Eq. (35):

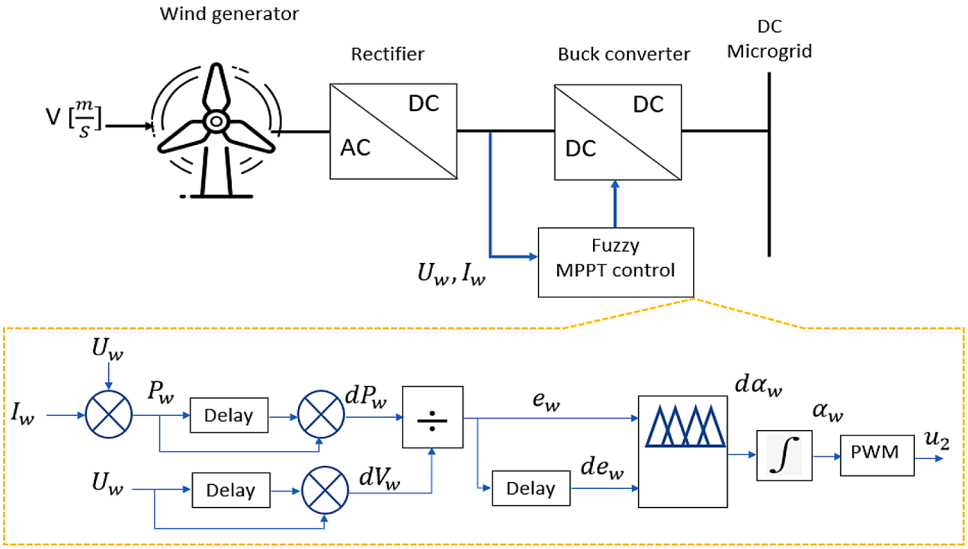

Fig. 9. MPPT control of wind source based FLC.

Table 2
Rules for wind fuzzy logic control.

e_k / de	NB	NS	ZE	PS	PB
NB	ZE	PB	ZE	NB	NS
NS	PS	ZE	ZE	NB	NS
ZE	ZE	ZE	ZE	ZE	ZE
PS	PS	PB	ZE	ZE	NS
PB	PS	PB	ZE	NB	ZE

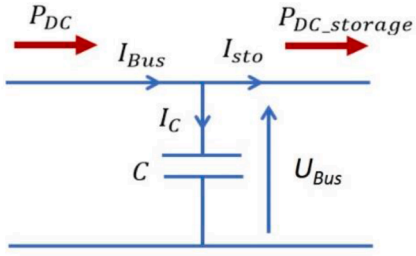

Fig. 10. Common DC bus.

$$e_k = \frac{P_{pv_{(k)}} - P_{pv_{(k-1)}}}{U_{pv_{(k)}} - U_{pv_{(k-1)}}} \tag{34}$$

$$d_e = e_{(k)} - e_{(k-1)} \tag{35}$$

where P_{pv} and U_{pv} are the power and voltage PV plant, respectively.

Fig. 8 illustrates the FLC principle applied to the boost converter. Table 1 presents the rules applied by the FLC in the inference phase, being the acronyms used negative big (NB), negative small (NS), zero (ZE), positive small (PS), positive big (PB). In the next step of the defuzzification process, the duty cycle variation is determined. The duty cycle ($\alpha_{(k)}$) of the boost converter control is obtained by Eq. (36).

$$\alpha_{(k)} = \Delta\alpha_{(k)} - \alpha_{(k-1)} \tag{36}$$

Such as for the PV source, the FLC to extract the maximum power from the wind source is applied to the buck converter (Fig. 9). The input variables of the FLC are *dP* and *dV* which are the variation of the wind power and the variation of the voltage at the input of the converter (Table 2), being the output of the FLC the duty cycle. The expressions of the FLC inputs are given by Eq. (37) and Eq. (38).

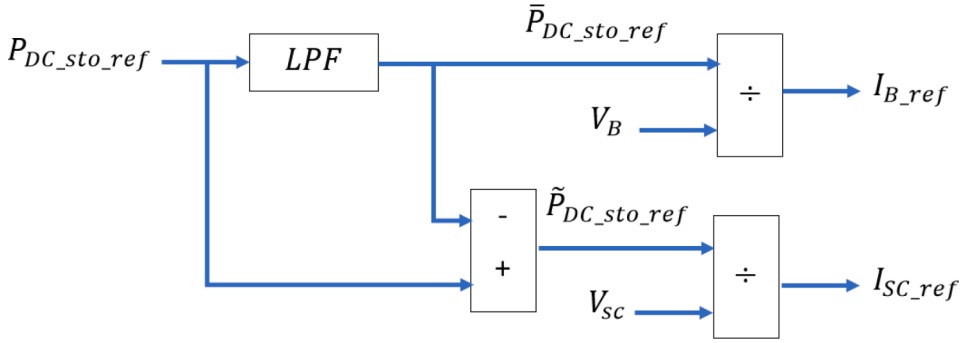

Fig. 11. Battery and supercapacitor current references.

$$e_k = \frac{P_{w_{(k)}} - P_{w_{(k-1)}}}{U_{w_{(k)}} - U_{w_{(k-1)}}} \tag{37}$$

$$d_e = e_{(k)} - e_{(k-1)} \tag{38}$$

where P_w and U_w are the power and voltage wind turbine, respectively.

4.2. DC bus control strategy

The DC bus regulation is a very important part of the energy management of the power flow delivered or collected by the DC bus (Fig. 10). The objective of DC bus regulation is to regulate the bus voltage at the appropriate level, defined as 400 V, to ensure an energy balance between production and consumption, share the surplus power or deficit with the batteries and the SC, and also direct the higher frequency components of the current to the SC. The bus voltage regulation consists of two loops. An external loop dedicated to the bus voltage regulation, and an internal loop for the battery and SC current regulation. The regulation of the bus voltage can be performed by several methods, in which is possible to mention the classical linear method using PID control or by innovative non-linear control methods such as FLC, SMC, among others. In this paper, the study is focused on the regulation of the DC bus voltage, the battery, and the capacitor currents by applying the SMC.

The DC bus is the common connection point of all the power converters. The power available in the DC bus (P_{DC}) is the difference between production (P_{SDC}) and the consumption (P_{LDC}) is expressed by Eq. (39):

$$P_{DC} = P_{S_{DC}} - P_{L_{DC}} \tag{39}$$

Considering the storage system and based on Fig. 10, which shows the power available in the DC bus and the power sent to the storages systems, the continuous common DC bus is described by the following relation:

$$C \cdot U_{Bus} \frac{dU_{Bus}}{dt} = U_{Bus} \cdot I_{Bus} - U_{Bus} \cdot I_{sto} \tag{40}$$

where $U_{BUS} \cdot I_{BUS}$ is the power available in the bus, $U_{BUS} \cdot I_{sto}$ is the power received or delivered by the storage devices. C is the equivalent capacity connected to the DC bus. From Eq. (40), is possible to obtain Eq. (41):

$$\frac{dx}{dt} = \frac{2 \cdot P_{DC}}{C} + \frac{2 \cdot P_{DC_{sto}}}{C} \tag{41}$$

The error between the bus voltage and reference is described as $e_1 = x - x_{ref}$, where x_{ref} is the square of the DC bus voltage reference. The derivative of the error is expressed using Eq. (42):

$$\frac{de_1}{dt} = \frac{2}{C} \cdot (P_{DC} - P_{DC_{sto}}) \tag{42}$$

The sliding surface (S_1) is defined as Eq. (43):

$$S_1 = e_1 + k_1 \int e_1 \tag{43}$$

where k_1 is a SMC design parameter ($k_1 > 0$). The derivative of the surface S_1 is given by the following expression:

$$\frac{dS_1}{dt} = \frac{2}{C} \cdot (P_{DC} - P_{DC_{sto}}) + k_1 \cdot e_1 \tag{44}$$

For Lyapunov stability ($S.\dot{S} < 0$) and convergence of the error to zero, the storage current reference is expressed by Eq. (45):

$$P_{DC_{sto_{ref}}} = P_{DC} + \frac{C}{2} \cdot k_2 sign(S) + \frac{C}{2} \cdot k_1 \cdot e_1 \tag{45}$$

Where k_2 is a SMC design parameter ($k_2 > 0$). The reference power is composed of two terms, in which the first term represents the average component of the power ($\widetilde{P}_{DC_{sto_{ref}}}$) and the other term is the power component for higher frequencies ($\overline{P}_{DC_{sto_{ref}}}$).

$$P_{DC_{sto_{ref}}} = \widetilde{P}_{DC_{sto_{ref}}} + \overline{P}_{DC_{sto_{ref}}} \tag{46}$$

The battery and the SC reference currents ($I_{B_{ref}}$ and $I_{SC_{ref}}$, respectively) are obtained from the shared power showed in Eqs. (47) and (48). Fig. 11 illustrates the principle of determining the I_B and I_{SC} current references.

$$I_{B_{ref}} = \frac{\widetilde{P}_{DC_{sto_{ref}}}}{U_{Bat}} \tag{47}$$

$$I_{SC_{ref}} = \frac{\widetilde{P}_{DC_{sto_{ref}}}}{U_{SC}} \tag{48}$$

4.3. Battery and supercapacitor current control

The error between the battery current (I_B) and reference (I_{Bref}) can be calculated in Eq. (49), while that the error between the SC current and reference is given by Eq. (50).

$$e_2 = I_B - I_{B_{ref}} \tag{49}$$

$$e_3 = I_{SC} - I_{SC_{ref}} \tag{50}$$

where the $I_{B_{ref}}$ is the battery reference current and $I_{SC_{ref}}$ is the SC reference current.

The derivative of the errors are expressed using Eqs. (51) and (52):

$$\frac{de_2}{dt} = \frac{U_{Bat}}{L_3} - \alpha_{34} \cdot \frac{U_{Bus}}{L_3} - \frac{dI_{B_{ref}}}{dt} \tag{51}$$

$$\frac{de_3}{dt} = \frac{U_{SC}}{L_4} - \alpha_{56} \cdot \frac{U_{Bus}}{L_4} - \frac{dI_{SC_{ref}}}{dt} \tag{52}$$

The sliding surface for battery and SC current control is given by Eq. (53) and (54), respectively.

$$S_2 = e_2 + k_3 \int e_2 \tag{53}$$

$$S_3 = e_3 + k_4 \int e_3 \tag{54}$$

where $k_3$and k_4 are a SMC design parameter ($k_3 > 0$, $k_4 > 0$).

The derivative of the surface S_2 and S_3 is given by the following Eq. (55) and (56):

$$\frac{dS_2}{dt} = \frac{U_{Bat}}{L_3} - \alpha_{34} \cdot \frac{U_{Bus}}{L_3} - \frac{dI_{B_{ref}}}{dt} + k_3 \cdot e_2 \tag{55}$$

$$\frac{dS_3}{dt} = \frac{U_{SC}}{L_4} - \alpha_{56} \cdot \frac{U_{Bus}}{L_3} - \frac{dI_{SC_{ref}}}{dt} + k_4 \cdot e_3 \tag{56}$$

For Lyapunov stability ($S \cdot \dot{S} < 0$) and convergence of the error to zero, the control law is expressed for a derivative of the sliding surface, represented by Eqs. (57) and (58):

$$\frac{dS_2}{dt} = -k_4 sign(S_2) \tag{57}$$

$$\frac{dS_3}{dt} = -k_5 sign(S_3) \tag{58}$$

where $k_4$and k_5 are a SMC design parameter ($k_4 > 0$), $k_5 > 0$).

From Eqs. (55) and (57), the battery current control law is given by Eq. (59), while from Eq, 56 and 58, the SC current control law is given by Eq. (60):

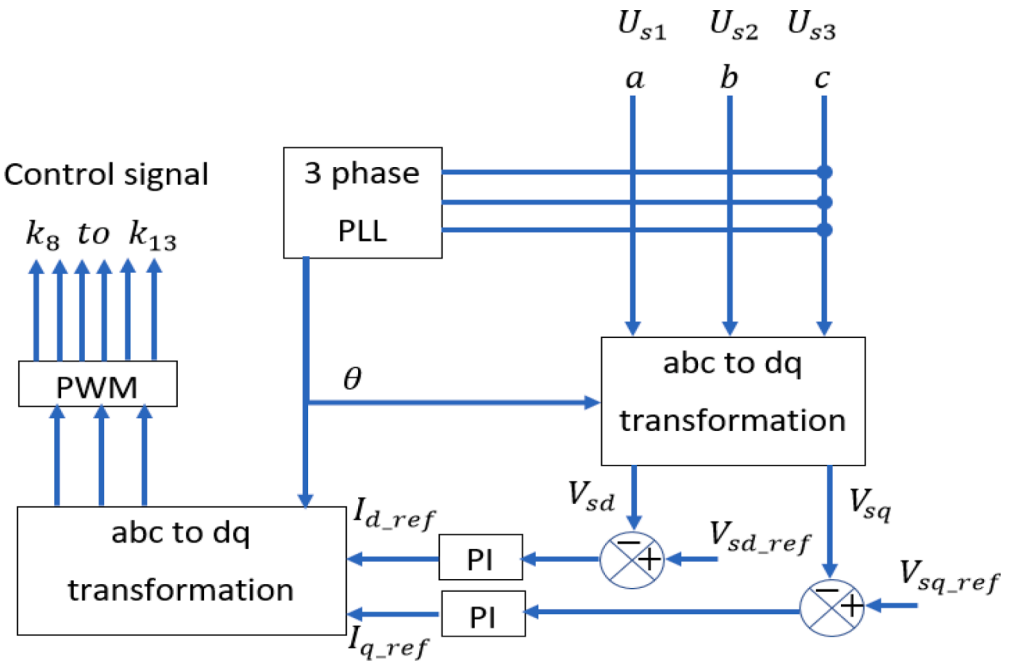

Fig. 12. Three phase inverter controller.

Table 3
System specifications.

Parameter	Value	Parameter	Value
PV generator		**Supercapacitor**	
Optimal PV power (P_{PVopt})	1492 W	Initial supercapacitor voltage (V_{SC_init})	209 V
Optimal PV voltage (U_{PVopt})	203 V	Supercapacitor rated capacity (C_{SC})	10 F
Optimal PV current (U_{PVopt})	7.35 A	**DC Bus**	
Open-circuit voltage (V_{oc})	254.1 V	DC bus voltage (V_{BUS})	400 V
Short circuit current (I_{sc})	7.84 A	Capacitor DC Bus (C_{BUS})	3000 μF
Wind turbine		**DC-DC converter**	
Power coefficient (Cp)	0.43	Inductors ($L_1 = L_2 = L_5$)	10 mH
Optimal wind power (P_{w_opt})	1520 W	Inductors ($L_3 = L_4$)	2 mH
Blade radius (R)	4 m	Resistance (R_s)	30 Ω
Battery		**DC-AC converter**	
Battery nominal voltage (V_{B_N})	215	Inductors (L_6)	3 mH
Battery rated capacity (C_B)	2 Ah	Maximum Voltage (V_{s_max})	150 V

$$\alpha_{34} = \frac{L_3}{U_{Bus}}\left[k_4 sign(S_2) + \frac{U_{Bat}}{L_3} - \frac{dI_{B_{ref}}}{dt} + k_3 \cdot e_2\right] \tag{59}$$

$$\alpha_{56} = \frac{L_4}{U_{SC}}\left[k_5 sign(S_3) + \frac{U_{SC}}{L_4} - \alpha_{34}\frac{U_{Bus}}{L_3} - \frac{dI_{SC_{ref}}}{dt} + k_4 \cdot e_3\right] \tag{60}$$

4.1. Control of DC and AC load terminal voltages

Depending on the user necessity, the voltage across the DC load is regulated to a voltage less than or equal to the DC bus voltage. This control allows a wide flexibility of DC loads to be connected to the DC microgrid. The error between the DC load voltage (U_L) and its reference, is given by Eq. (61):

$$e_4 = U_L - U_{L_{ref}} \tag{61}$$

$U_{L_{ref}}$ is the reference voltage of the DC load.
The derivative of the error is expressed using Eq. (62).

$$\frac{de_4}{dt} = \alpha_7 \cdot I_{DC} - \frac{U_L}{R_L} \tag{62}$$

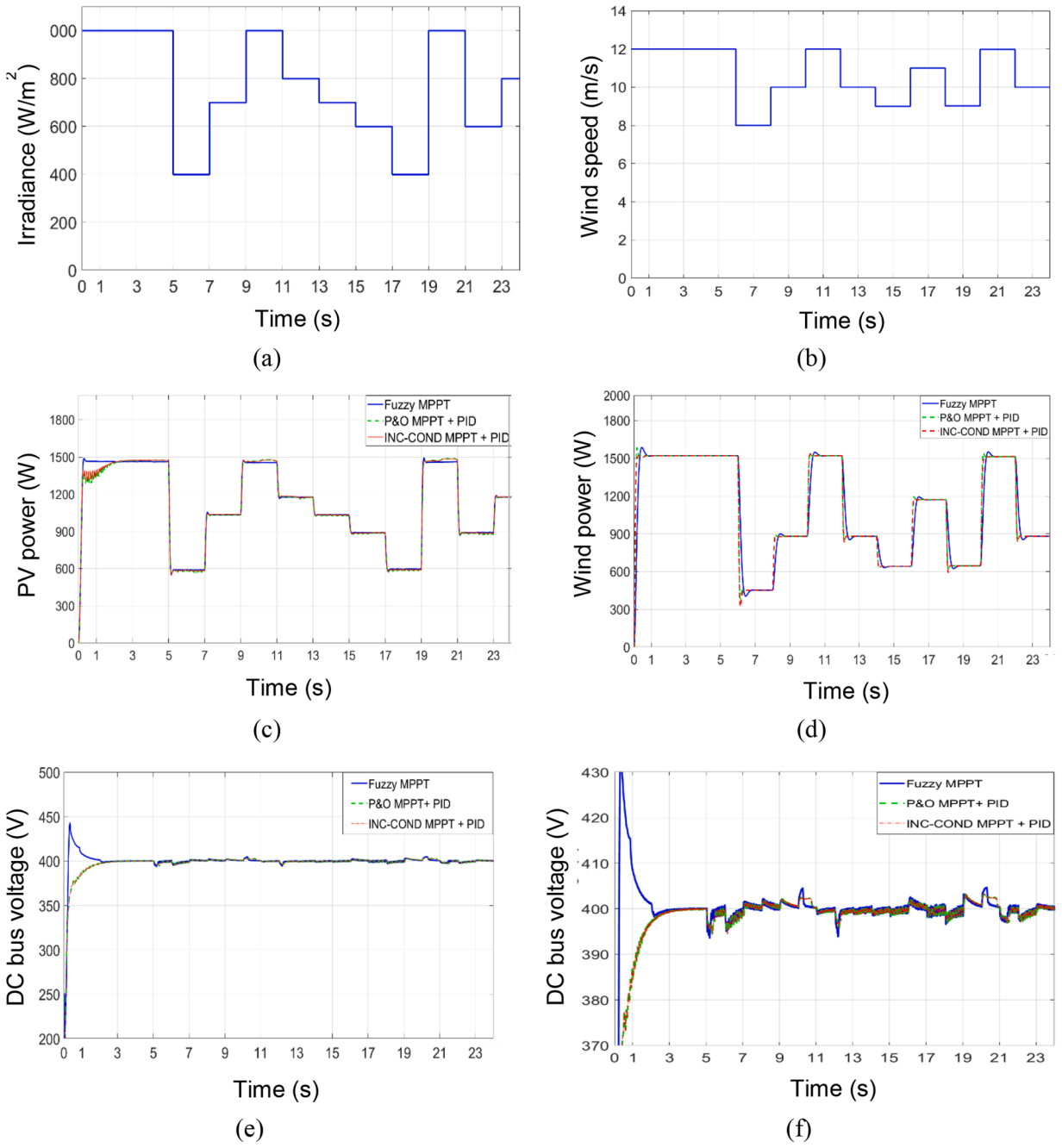

Fig. 13. Case 1 - a) Irradiation; b) Wind speed; c) PV power; d) Wind power; e) DC bus voltage; f) Zoom of the DC bus voltage.

The sliding surface, is given by:

$$S_4 = e_4 + k_6 \int e_4 \tag{63}$$

Where k_6 is a SMC design parameter ($k_6 > 0$).
The derivative of the surface S_4 is given by the Eq. (64):

$$\frac{dS_4}{dt} = \alpha_7 \cdot I_{DC} - \frac{U_L}{R_L} + k_6 \cdot e_4 \tag{64}$$

For Lyapunov stability ($S.\dot{S} < 0$) and convergence of the error to zero, the control law is expressed for a derivative of the sliding

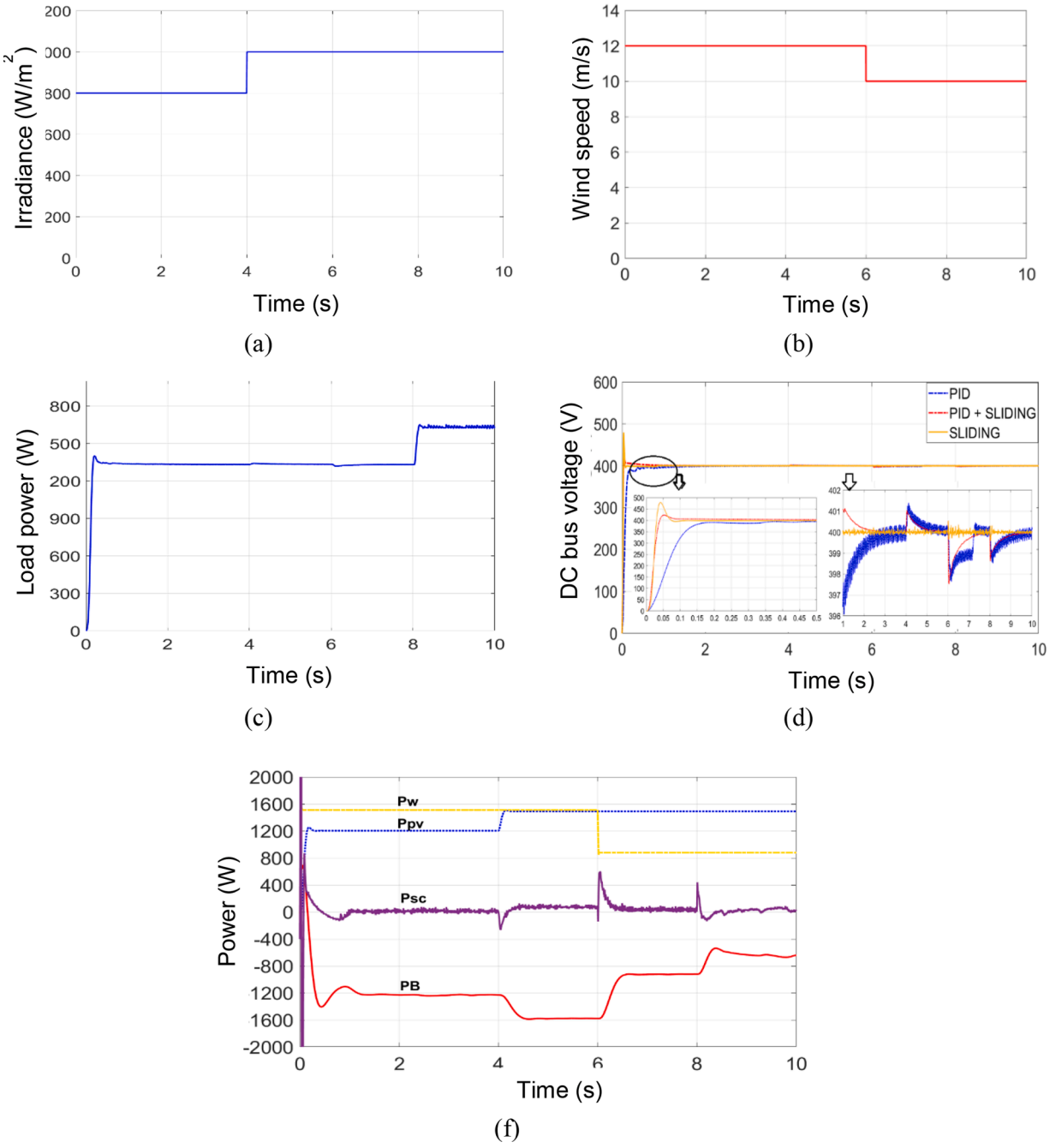

Fig. 14. Case 2 - a) Irradiance; b) Wind speed; c) Load power change; d) DC Bus voltage; e) Wind, PV, battery and supercapacitor powers.

surface equal to:

$$\frac{dS_4}{dt} = -k_7 \cdot sign(S_4) \tag{65}$$

k_7 is a SMC design parameter ($k_7 > 0$).
Using Eqs. (64) and (65), the control law is given by the following Eq. (66):

$$\alpha_7 = \frac{C_S}{I_{DC}}\left[- k_8 sign(S_4) + \frac{U_L}{R_S \cdot C_S} - k_7 \cdot e_4 \right] \tag{66}$$

The three-phase inverter is inserted between the DC bus and the AC load. The control objective of this converter is to obtain a three-

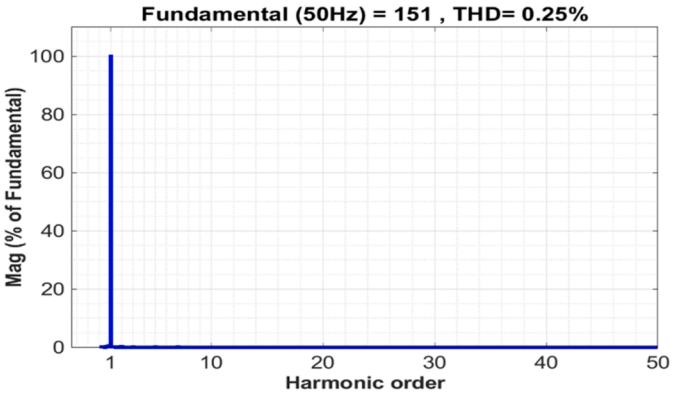

Fig. 15. Total harmonic distortion of the AC line voltage.

phase system with a maximum value of 150 V and a frequency of 50 Hz while minimizing the distortion rate. The control principle of the three-phase inverter is based on the *dq* transformation which delivers two components, one direct and the other in quadrature for the voltage and current vectors [24]. An external loop is dedicated to the regulation of the dq voltage components and another internal loop ensures the regulation of the dq current components. In order to simplify, the current loop is not shown in Fig. 12. A *PLL* (phase locked loop) detects the phase used to determine the *dq* components based on the use of a rotating reference frame. This control principle is called vector control whose principle is identical to the control of electrical machines. The control principle of the three-phase inverter is given in Fig. 12.

5. Simulation results

The energy management method (Fig. 5) and control strategy (Fig. 6) discussed in the previous sections are simulated using the Matlab/Simulink® platform. The simulation parameters are given in Table 3. The simulations were performed considering two cases, being the first one considering a variation of irradiation and wind speed, and the second considering a variation of power demanded by the load.

Case 1: Irradiation and wind speed variation

In case 1 is considered constant DC and AC load, and the objective is to compare the performance of three MPPT algorithms: FLC, IN-COND, and P&O. The solar irradiation profile is given in Fig. 13a. The solar irradiation intensity varies between 400 W/m^2 and 1000 W/m^2. The wind profile is given in Fig. 13b, where it is possible to observe a variation between 8 m/s and 12 m/s.

The respective PV power generated according to the irradiation profile is given in Fig. 13c. The power of 1490 W corresponds to the maximum power for a 1000 W/m^2 irradiation and a temperature of 25°C. For the control of photovoltaic power in the transient state, it is noticed that the three algorithms find the optimal point in less than 1s (Fig. 13c). According to these results, it can be concluded that the three algorithms ensure maximum power point tracking with almost identical tracking performance. A small difference between these algorithms is observed in the transient regime, in which the MPPT based on FLC is faster, detecting the optimal point in less than 0.5 s (Fig. 13c).

For the control of wind power, in steady state and for a wind speed of 12 m/s, the wind power is equal to 1520 W for the three algorithms (Fig. 13d). It is concluded that there is no significant difference between the performances of these algorithms. These MPPT are suitable for use in DC microgrids and allow better tracking of the maximum power point despite the relatively high speed change of the wind profile. To conclude, the efficiency of the MPPT algorithms are almost unitary. According to the manufacturer's specifications and the simulations performed the energy production of the photovoltaic and wind turbine sources, for the irradiation and wind speed levels, proof that these generators provide their maximum power.

Fig. 13e shows the DC bus voltage. The bus voltage is regulated to its reference value of 400V, and this voltage is shown for the MPPT algorithms reported earlier. For all MPPTs, the voltage returns to its reference value after 2s of the transient period. During changes in irradiation and wind speed, the power injected into the DC bus changes. The DC voltage on this bus varies slightly, as seen in Fig. 13e. However, the DC voltage remains in adequate levels. It is noted when using the FLC MPPT, the maximum deviation recorded is equal to 6.5V at t = 5.1 s, whereas the maximum deviation recorded when using the P&O/INC-COND algorithms is equal to 5 V at t = 5.1 s. Considering these facts, it is possible to conclude that despite the application of rapid variations in wind speed and solar irradiation, the DC bus voltage follows the set point of 400 V. In other words, the bus voltage is not very sensitive to abrupt climate variations and it is kept stable around its reference value (Fig. 13f).

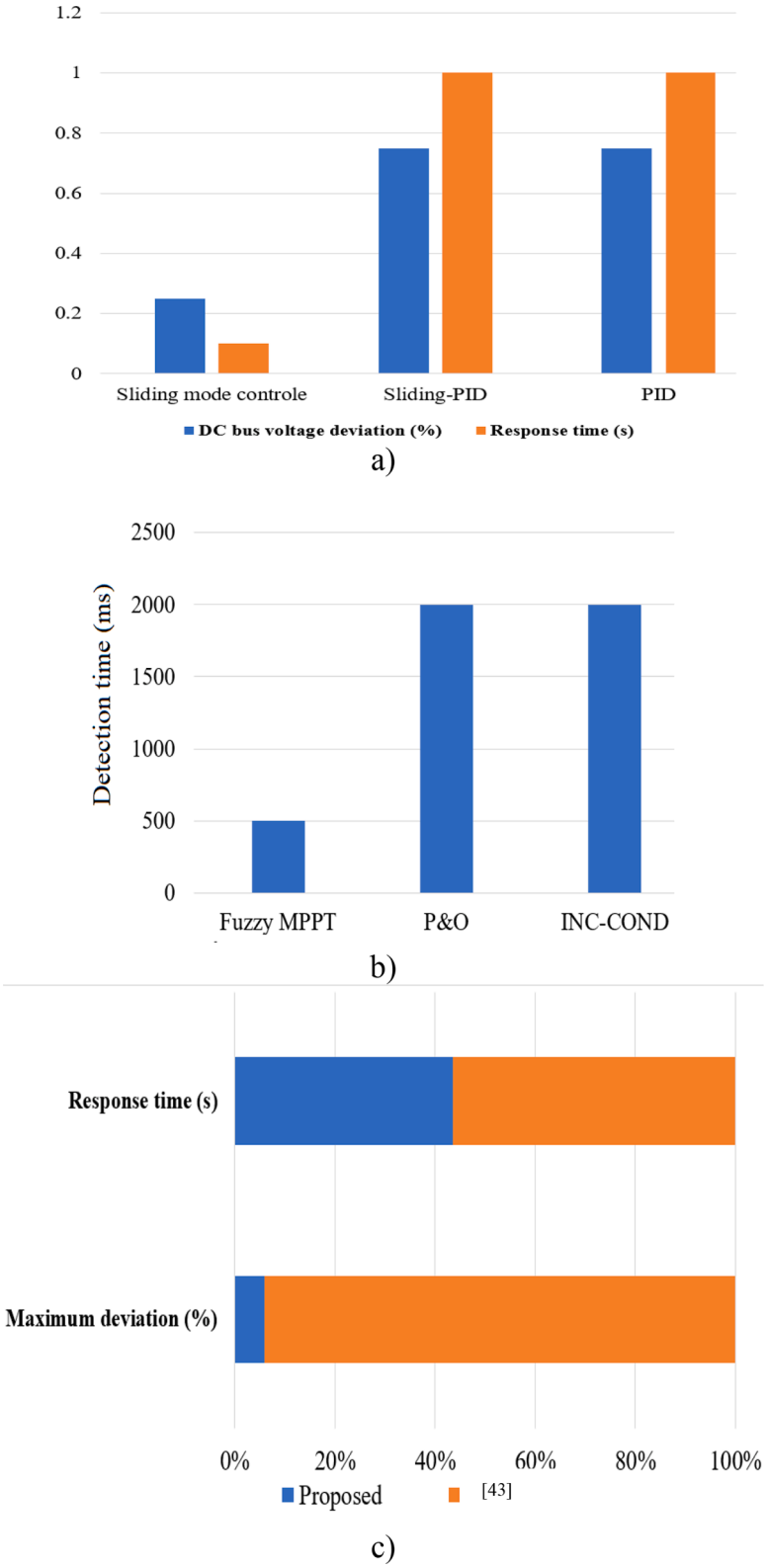

Fig. 16. Performance comparison. a) Control strategy; b) MPPT algorithm detection time; c) Maximum voltage deviation and response time for DC bus.

Case 2: Irradiation step, wind speed step and load power change

In Case 2, the microgrid system is submitted to three successive changes, an increase in irradiance (Fig. 14a) from 800 W/m^2 to 1000 W/m^2 at t = 4s, a decrease in wind speed (Fig. 14b) from 12 m/s to 10 m/s at t = 6s, and an increase in power absorbed by the DC and AC loads from 1330 W to 1600 W at t = 8s (Fig. 14c). The temperature is maintained at 25°C. The objective in this case is to evaluate the performance of the control methods: (i) SMC, (ii) PID, and (iii) PID-SMC. At the simulation start time, the irradiation is equal to 800 W/m^2, the wind speed is 12 m/s, and the power consumed by the load is 1330 W. Fig. 14d shows the DC bus voltage. It is noticed that the DC bus voltage finds the reference in less than 0.1s for the SMC method. In contrast, the time necessary for the PID and PID-SMC is 1s. If the comparison criteria are response or tracking time, the SMC offers an improved response speed with 10 times less tracking time. In steady state, the SMC control method allows a more stable response with small or negligible deviations around the reference compared to other control methods. Contrary to the SMC control, it is possible to notice that the deviation of the DC bus voltage is more evident for the PID and PID–SMC. This deviation reaches 3V in the case of PID and PID–SMC, which corresponds to a relative deviation of 0.75%. In contrast, this deviation is less than 1V in the case of SMC, which corresponds to a relative deviation of 0.25% of the DC bus voltage, thus being three times smaller. From the above results, it is concluded that the SMC allows regulation of the DC bus voltage with the lowest deviation around its reference, in comparison with the other methods. Fig. 14e illustrates the different powers of the DC microgrid. Four intervals are distinguished:

- During the time interval from 0 to 4s, the PV and wind generator provide a power of 1.2 kW and 1.52 kW, respectively. The power fluctuations are directed at the SC. The battery charges in this time interval with a power of 1.22kW. In principle, if the power consumption of the DC and AC loads is subtracted from the power generated by the PV and wind systems, the remaining power is equal to 1.39 kW. This power is the effective power delivered by the storage devices in the DC bus. The difference between the power of the storage devices and the power available on the DC bus represents the losses in the static converters. The power losses are equal to 175 W (1.39 kW - 1.22 kW). These losses represent 6.4 % of the total power produced.
- During the time interval from 4 to 6s, the PV generator power increases and reaches its peak power of 1.49 kW. The wind power remains at the same value of 1.52 kW. The total produced power is equal to 3.01 kW. The increase in the photovoltaic power causes a power fluctuation in the DC bus, which is intercepted by the SC at time t = 4s. The DC and AC loads consume 1.33 kW. The power directed to charge the battery is equal to 1.6 kW, making this power bigger than the first time interval, since an increase is noted in the PV power. The low frequency current component is directed to charge the battery, which guarantees low stress for this device. The high frequency current component is directed to the SC. The power available on the DC bus is equal to 1.41 kW. The difference between the available power and the battery charging power represents the losses in the static converters. The power losses are equal to 190 W. These losses represent 6.3% of the total power produced. The same remarks are made for the remaining time of the simulation.

To conclude, the proposed energy management method ensures better speed and regulation of the DC bus voltage with maximum deviations of approximately 1V (0.25%), therefore ensuring compliance with the standard IEEE std-519-1992 of +/-5 % allowed limit.

Fig. 15 illustrates the total harmonic distortion (THD) spectrum of the AC voltage destined to supply the AC load. The fundamental of the AC voltage has a frequency of 50 Hz and is regulated at 151V with a distortion rate of 0.25%.

In Fig. 16, the results obtained by this paper are summarized. Fig. 16a shows the performance of the SMC in terms of speed and maximum deviation of the DC bus voltage. It can be concluded that the SMC offers better performance than the other control methods. Regarding the MPPT algorithms in Fig. 16b, all the control methods allow the maximum power point tracking with almost the same performance. The FLC was characterized by an optimal detection time, four times lower than the other MPPT algorithms. Fig. 16c shows the results of the proposed method in comparison with the results in [43]. This figure shows that the deviation in the DC bus obtained in the present paper reached a lower deviation with an improved response time.

5. Conclusions

In this paper, a microgrid system based on PV source, wind generator, battery, supercapacitor, and AC/DC loads operating in autonomous mode are studied. The modeling of the constituent elements of the microgrid, based on the average equivalent model, are presented. Three MPPT methods (INC-COND, P&O, and FLC) are performed in order to maximize the power extracted from the PV and wind sources. The simulation results show the superiority of the FLC MPPT compared to the other conventional methods. The storage devices are controlled in order to meet the energy demand and ensure a balance between energy production and consumption. The batteries and supercapacitor are controlled through a bidirectional current converter, in which the high frequency power components are directed to the supercapacitor, contributing to increasing the battery life and meeting the transient energy needs. Energy management and control are performed using sliding mode control in order to achieve a balance between energy production and demand. Stability was ensured in the application of the SMC by the Lyapunov theorem. The proposed control method proved to perform better, since the reference value was reached three times faster compared to PID and PID-SMC. Another improvement is recorded in the three-phase inverter control that produces a sinusoidal voltage with a fundamental amplitude of 150 V and a frequency of 50 Hz. A lower distortion is recorded compared to another paper in the literature (THD = 0.25%). It is important to emphasize that the energy management strategy presents limitations in particular cases, such as the full discharge or full load of storage devices below or above selected limits. This limitation can be solved by storage system expansion or connecting the microgrid system to the utility grid, thus allowing flexible energy management and guaranteeing a balance between production and consumption, without the need to stop the MPPT control of the renewable resources.

Data availability

No data was used for the research described in the article.

References

[1] R. Inglesi-Lotz, The impact of renewable energy consumption to economic growth: a panel data application, Energy Econ. 53 (2016) 58–63, https://doi.org/10.1016/j.eneco.2015.01.003.
[2] A. Shrestha, A.A. Mustafa, M.M. Htike, V. You, M. Kakinaka, Evolution of energy mix in emerging countries: modern renewable energy, traditional renewable energy, and non-renewable energy, Renew. Energy 199 (December 2021) (2022) 419–432, https://doi.org/10.1016/j.renene.2022.09.018.
[3] N. Ilechukwu, S. Lahiri, Renewable-energy consumption and international trade, Energy Rep. 8 (2022) 10624–10629, https://doi.org/10.1016/j.egyr.2022.08.209.
[4] E.I. Come Zebra, H.J. van der Windt, G. Nhumaio, A.P.C. Faaij, A review of hybrid renewable energy systems in mini-grids for off-grid electrification in developing countries, Renew. Sustain. Energy Rev. 144 (April) (2021), https://doi.org/10.1016/j.rser.2021.111036.
[5] M. Abbasi, A.G. Garganeev, Hybrid microgrid in islanded operation based on renewable energy sources, in: Int. Conf. Young Spec. Micro/Nanotechnologies Electron Devices, EDM 2018-July, 2018, pp. 555–559, https://doi.org/10.1109/EDM.2018.8434949.
[6] Y. Shi, Y. Sun, J. Liu, X. Du, Model and stability analysis of grid-connected PV system considering the variation of solar irradiance and cell temperature, Int. J. Electr. Power Energy Syst. 132 (2021), https://doi.org/10.1016/j.ijepes.2021.107155.
[7] T. Ma, H. Yang, L. Lu, Study on stand-alone power supply options for an isolated community, Int. J. Electr. Power Energy Syst. 65 (2015) 1–11, https://doi.org/10.1016/j.ijepes.2014.09.023.
[8] J.K. Kaldellis, I. Ninou, Energy balance analysis of combined photovoltaic-diesel powered telecommunication stations, Int. J. Electr. Power Energy Syst. 33 (10) (2011) 1739–1749, https://doi.org/10.1016/j.ijepes.2011.08.016.
[9] H. Abouobaida, S. El Bied, New optimization method of the MPPT algorithm and balancing voltage control of the Three-Level Boost Converter (TLBC, Int. J. Appl. Power Eng. 6 (2) (2017) 113, https://doi.org/10.11591/ijape.v6.i2.pp113-122.
[10] H. Abouobaida, S.EL Beid, The ripple correlation optimal point determination in a medium power wind conversion system and performance evaluation with respect to conventional algorithms, modeling, identification and control methods in renewable energy systems. Green Energy and Technology, Springer, Singapore, 2019, pp. 131–150, https://doi.org/10.1007/978-981-13-1945-7_6.
[11] A.I.M. Ali, H.R.A. Mohamed, Improved P&O MPPT algorithm with efficient open-circuit voltage estimation for two-stage grid-integrated PV system under realistic solar radiation, Int. J. Electr. Power Energy Syst. 137 (December 2021) (2022), 107805, https://doi.org/10.1016/j.ijepes.2021.107805.
[12] K.S. Tey, S. Mekhilef, Modified incremental conductance MPPT algorithm to mitigate inaccurate responses under fast-changing solar irradiation level, Sol. Energy 101 (2014) 333–342, https://doi.org/10.1016/j.solener.2014.01.003.
[13] G.Mathew Kurian, P.Aruna Jeyanthy, D. Devaraj, FPGA implementation of FLC-MPPT for harmonics reduction in sustainable photovoltaic system, Sustain. Energy Technol. Assessments 52 (PC) (2022), 102192, https://doi.org/10.1016/j.seta.2022.102192.
[14] H. Doubabi, I. Salhi, M. Chennani, N. Essounbouli, High performance MPPT based on TS fuzzy–integral backstepping control for PV system under rapid varying irradiance—experimental validation, ISA Trans. (xxxx) (2021), https://doi.org/10.1016/j.isatra.2021.02.004.
[15] M.A. Abdullah, A.H.M. Yatim, C.W. Tan, R. Saidur, A review of maximum power point tracking algorithms for wind energy systems, Renew. Sustain. Energy Rev. 16 (5) (2012) 3220–3227, https://doi.org/10.1016/j.rser.2012.02.016.
[16] J. Shair, H. Li, J. Hu, X. Xie, Power system stability issues, classifications and research prospects in the context of high-penetration of renewables and power electronics, Renew. Sustain. Energy Rev. 145 (April) (2021), 111111, https://doi.org/10.1016/j.rser.2021.111111.
[17] A.G. Olabi, C. Onumaegbu, T. Wilberforce, M. Ramadan, M.A. Abdelkareem, A.H. Al – Alami, Critical review of energy storage systems, Energy 214 (Jan. 2021), 118987, https://doi.org/10.1016/j.energy.2020.118987.
[18] A. Kadri, H. Marzougui, A. Aouiti, F. Bacha, Energy management and control strategy for a DFIG wind turbine/fuel cell hybrid system with super capacitor storage system, Energy 192 (2020), 116518, https://doi.org/10.1016/j.energy.2019.116518.
[19] L. Barelli, G. Bidini, P. Cherubini, A. Micangeli, D. Pelosi, C. Tacconelli, How hybridization of energy storage technologies can provide additional flexibility and competitiveness to microgrids in the context of developing countries, Energies 12 (16) (2019), https://doi.org/10.3390/en12163138.
[20] X. Liu, P. Wang, and P. C. Loh, "A hybrid AC /DC microgrid and its," vol. 2, no. 2, pp. 278–286, 2011.
[21] S. Sinha, P. Bajpai, Power management of hybrid energy storage system in a standalone DC microgrid, J. Energy Storage 30 (June) (2020), 101523, https://doi.org/10.1016/j.est.2020.101523.
[22] L. de Oliveira-Assis, E.P.P. Soares-Ramos, P. García-Triviño, R. Sarrias-Mena, C.A. García-Vázquez, L.M. Fernández-Ramírez, Fuzzy-based energy management system for a MVDC PV power plant with battery stored Quasi-Z-source inverter, in: 21st IEEE Int. Conf. Environ. Electr. Eng. 2021 5th IEEE Ind. Commer. Power Syst. Eur. EEEIC /I CPS Eur. 2021 - Proc, 2021, https://doi.org/10.1109/EEEIC/ICPSEurope51590.2021.9584829.
[23] P. Singh, J.S. Lather, Dynamic power management and control for low voltage DC microgrid with hybrid energy storage system using hybrid bat search algorithm and artificial neural network, J. Energy Storage 32 (March) (2020), 101974, https://doi.org/10.1016/j.est.2020.101974.
[24] P. Singh, J.S. Lather, Power management and control of a grid-independent DC microgrid with hybrid energy storage system, Sustain. Energy Technol. Assessments 43 (November 2020) (2021), 100924, https://doi.org/10.1016/j.seta.2020.100924.
[25] A. T. Azar and Q. Zhu, Eds., *Advances and Applications in Sliding Mode Control systems*, vol. 576. Cham: Springer International Publishing, 2015.
[26] H.H.H. Mousa, A.R. Youssef, E.E.M. Mohamed, State of the art perturb and observe MPPT algorithms based wind energy conversion systems: a technology review, Int. J. Electr. Power Energy Syst. 126 (PA) (2021), 106598, https://doi.org/10.1016/j.ijepes.2020.106598.
[27] H. Taghavifar, H. Taghavifar, Adaptive robust control-based energy management of hybrid PV-battery systems with improved transient performance, Int. J. Hydrogen Energy 46 (10) (2021) 7442–7453, https://doi.org/10.1016/j.ijhydene.2020.11.243.
[28] L. de Oliveira-Assis, et al., Simplified model of battery energy-stored quasi-Z-source inverter-based photovoltaic power plant with Twofold energy management system, Energy 244 (2022), https://doi.org/10.1016/j.energy.2021.122563.
[29] B.S. Sami, N. Sihem, Z. Bassam, Design and implementation of an intelligent home energy management system: a realistic autonomous hybrid system using energy storage, Int. J. Hydrogen Energy 43 (42) (2018) 19352–19365, https://doi.org/10.1016/j.ijhydene.2018.09.001.
[30] S. Sivakumar, M.J. Sathik, P.S. Manoj, G. Sundararajan, An assessment on performance of DC-DC converters for renewable energy applications, Renew. Sustain. Energy Rev. 58 (2016) 1475–1485, https://doi.org/10.1016/j.rser.2015.12.057.
[31] A. Yazdani and R. Iravani, *Voltage Source Converters in Power Systems Modeling, Control and Applications*. 1377.
[32] "Generalized average model for a high-frequency link grid-connected DC_AC converter.pdf." .
[33] M. Li, X. Wu, S. Huang, G. Liang, Model predictive direct power control using optimal section selection for PWM rectifier with reduced calculation burden, Int. J. Electr. Power Energy Syst. 116 (2020), https://doi.org/10.1016/j.ijepes.2019.105552.
[34] W. De Soto, S.A. Klein, W.A. Beckman, Improvement and validation of a model for photovoltaic array performance, Sol. Energy 80 (1) (2006) 78–88, https://doi.org/10.1016/j.solener.2005.06.010.
[35] M.G. Villalva, J.R. Gazoli, E.R. Filho, Comprehensive approach to modeling and simulation of photovoltaic arrays, IEEE Trans. Power Electron. 24 (5) (2009) 1198–1208, https://doi.org/10.1109/TPEL.2009.2013862.
[36] S. Heier, Grid Integration of Wind Energy: Onshore and Offshore Conversion Systems, third ed., 2014.
[37] A. Rolan, A. Luna, G. Vazquez, D. Aguilar, G. Azevedo, Modeling of a variable speed wind turbine with a permanent magnet synchronous generator, in: 2009 IEEE International Symposium on Industrial Electronics 7, Jul. 2009, pp. 734–739, https://doi.org/10.1109/ISIE.2009.5218120.

[38] S. Ould Amrouche, D. Rekioua, T. Rekioua, S. Bacha, Overview of energy storage in renewable energy systems, Int. J. Hydrogen Energy 41 (45) (2016) 20914–20927, https://doi.org/10.1016/j.ijhydene.2016.06.243.
[39] R. Dufo-López, T. Cortés-Arcos, J.S. Artal-Sevil, J.L. Bernal-Agustín, Comparison of lead-acid and Li-ion batteries lifetime prediction models in stand-alone photovoltaic systems, Appl. Sci. 11 (3) (2021) 1–16, https://doi.org/10.3390/app11031099.
[40] A.B. Cultura, Z.M. Salameh, Modeling, evaluation and simulation of a supercapacitor module for energy storage application, Proc. Int. Conf. Comput. Inf. Syst. Ind. Appl. 18 (Cisia) (2015) 876–882, https://doi.org/10.2991/cisia-15.2015.235.
[41] Y. Shen, Z. Qin, H. Wang, O. F. A. B. D. Converter, Modeling and Control of DC-DC Converters, Elsevier Inc., 2018.
[42] W. Jianhua, Z. Fanghua, and G. Chunying, "Modeling and analysis of a buck /boost bidirectional converter with developed PWM switch model," 2011.
[43] P. Singh, J.S. Lather, Power management and control of a grid-independent DC microgrid with hybrid energy storage system, Sustain. Energy Technol. Assessments 43 (July 2020) (2021), 100924, https://doi.org/10.1016/j.seta.2020.100924.